Supporting Information

Photocatalytic H_2O Overall Splitting into H_2 Bubbles by Single Atomic Sulfur Vacancy CdS with Spin Polarization Electric Field

Jiari He,[†] Lijun Hu,[†] Chengtian Shao,[§] Shujuan Jiang,[†] Chuanzhi Sun,*[‡] Shaoqing Song*[†]*

[†]School of Material Science and Chemical Engineering, Ningbo University, Fenghua Road 818, Ningbo 315211, PR China

[‡]College of Chemistry, Chemical Engineering and Materials Science, Shandong Provincial Key Laboratory of Clean Production of Fine Chemicals, Shandong Normal University, Jinan 250014, PR China

[§]Department of Chemistry, Chung Yuan Christian University, Taoyuan City 32033, Taiwan

CONTENT LIST

EXPERIMENTAL SECTION.

Characterization. Microscopic morphology and lattice fringes of materials were observed with STEM (Titan G2, FEI); EPR was performed on an Elexsys E580e spectrometer (Bruker) that was operating at X-band (9.5 GHz) and utilizing a standard TE102 resonator with an ESR900 flow cryostat (Oxford Instruments). XPS was recorded by electron spectrometer (ESCALAB 210, VG, UK). XRD was investigated by D8 Focus X-ray diffractometer. Hall parameters were tested by using an Accent HL 5500 Hall system with a magnetic field of 0.5 T, electric current of 20 mA at 300 K. Apparent quantum yield was obtained by the photocatalytic quantum yield measurement system (PLD-QY1000). UV-vis spectrophotometer (UV-2600, Shimadzu, Japan) was used to give the UV-vis DRS patterns. FLS920 fluorescence lifetime spectrophotometer (Edimburgh Instruments) and RF-6000 (Hitachi, Japan) spectrophotometer were used to examine electron transfer dynamics and PL emission. All photoelectrochemical properties were tested on electrochemical workstation (CHI 760D Chenhua Instrument) with Na_2SO_4 as electrolyte solutions. Inductively Coupled Plasma Optical Emission Spectrometer (ICP-OES) data were obtained on Varian 720.

Photocatalytically splitting H_2O into H_2 fuel test. The photocatalytic H_2O splitting into H_2 fuel experiments were implemented in a three-neck Pyrex flask of 150 mL with natural sunlight or Xe lamp as light source using filter of above 420 nm (XQ350W, Lan Sheng Technology Co. Ltd. China). Photocatalyst (20 mg) was dispersed in 100 mL distilled water 8.45 g $Na_2S·9H_2O$ and 3.2 g Na_2SO_3 as sacrificial agents. Then nitrogen was introduced to flow continuously through the system for 30 min to remove the dissolved air. After irradiated for 30 min, H_2 released from the system was detected by chromatograph (Shimadzu, TCD). Apparent quantum efficiency was tested from PLR-QY1000 system.

Photocatalytically overall splitting H_2O into H_2 and O_2 tests. H_2O overall splitting reaction over samples were conducted with conditions similar to the above half reaction process but without sacrificial agents. Photocatalyst of 20 mg was dispersed into 100 mL H_2O by stirring and visible light of $\geqslant$ 420 nm was adopted as light source.

DFT calculation methods. Periodic DFT calculations were performed with the Perdew-Burke-Ernzerhof (PBE) exchange-correlation functional[S1] and the projector-augmented wave (PAW) method.[S2,S3] The Vienna *ab Initio* Simulation Program (VASP) package was used for the calculations in this work.[S4,S5] The geometry models optimized by B3LYP DFT. The Monkhorst-

Pack k-point meshes were set as 2×2×1, 2×2×2 and 2×2×3, separately. The recommended default potentials were employed for Cd and S element. An energy cutoff of 400 eV was used throughout this work, and spin polarization was also considered. Gaussian smearing with a width of 0.05 eV was applied. The electronic energy of the supercell was converged to 10^{-6} eV in the self-consistent field calculations, whereas the force on each relaxed atom was converged to 0.02 eV/Å in the ionic relaxation calculations. Corrections to the potential and forces was considered for CdS bulk structures with S vacancy, and the dipole moment along z direction was calculated. And the charge density difference for the formation of S vacancy on CdS bulk was calculated by $\rho_{diff} = \rho_{s\text{-}vac} + \rho_s - \rho_{total}$, in which $\rho_{s\text{-}vac}$ is the charge density distribution of CdS bulk with one S vacancy, ρ_s is the charge density distribution of S atom, and ρ_{total} is the charge density distribution of the entire CdS bulk.

FIGURES AND TABLES.

XRD profiles confirm the hexagonal crystal phase of all the prepared CdS NRs, as presented by the typical diffraction peaks for (101), (100), (110), (002) and (103) at 28.18˚, 24.81˚, 43.68˚, 26.51˚ and 47.84˚,[23,24 in the main text] respectively (Figure S1a). The degree of crystallization is improved as increasing the post-treating temperature. The lattice space of the exposed crystal plane was measured to be 0.336 nm both in HRTEM and HAADF-STEM images (Figure S1b), which corresponds to (002) crystal plane, and also FFT result confirms this information (Figure S1c). Therefore, a multi-layer model for (002) crystal plane of CdS was given as Figure S1d.

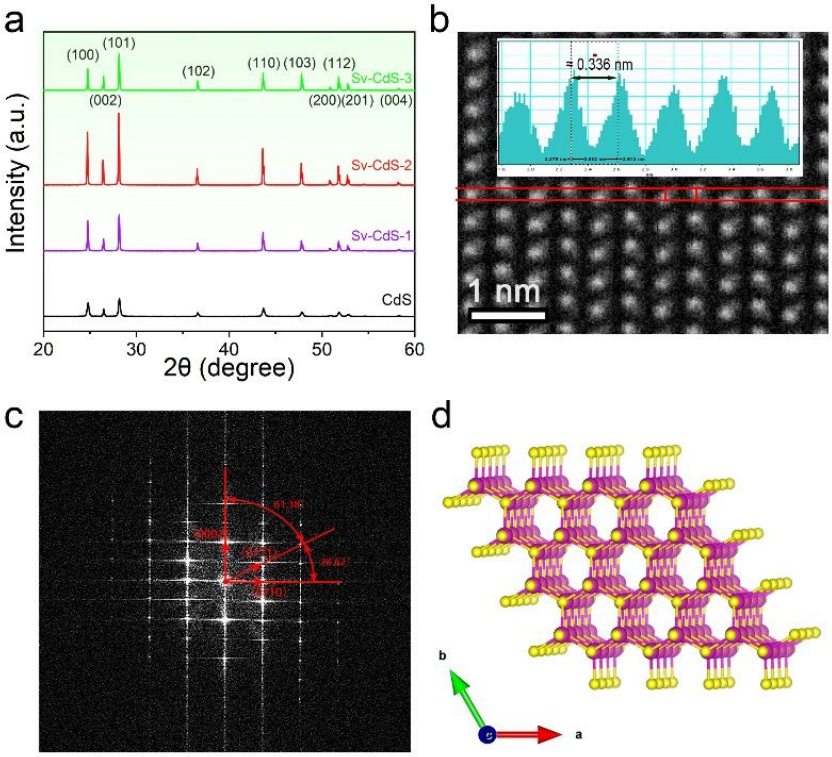

Figure S1. Structural information of CdS samples. (a) XRD patterns. (b) HAADF-STEM image and the measured crystal plane distance. (c) FFT image based on HAADF-STEM image. (d) Multi-layer model for (002) plane of hexagonal CdS.

With heating treatment to 800 °C, the rod shape of CdS remains unchanged, but the edge becomes more and more irregular, as shown in FESEM images of Figure S2a, e&i of the three Sv-CdS samples. The change of morphology is reflected as the gradual appearance of the irregular dark area near the surface of Sv-CdS with ~ten atom layer depth in ADF images. It is seen that intensities of Cd atom columns in Sv-CdS-2 have no much difference between the surface (Figure S2h) and bulk phase (Figure S3a-e). Comparatively, intensities of S atom columns gradually decrease as the detection line gets closer to surface, and this trend is intensified with increasing the treatment temperature (Figure S2d, h&l); even some S and Cd atoms in bulk phase detach after 900 °C treatment (Figure S3f-j), forming Cd-S multi-atomic vacancies. Therefore, single atomic S vacancies have been introduced into the surface of CdS with different contents, which will induce the spin polarization characteristic across Sv-CdS system due to the unpaired electrons.

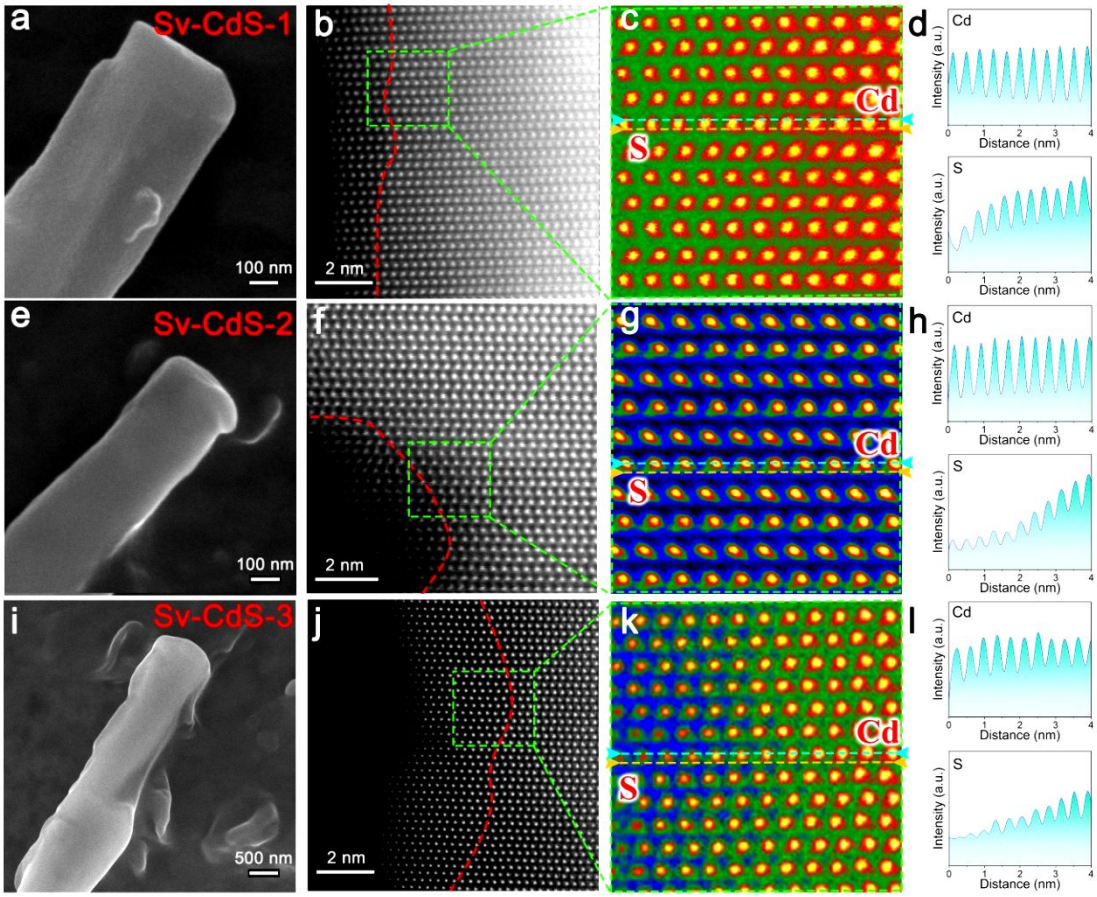

Figure S2. Morphology observation and structure analysis. (a, e, i) FESEM images. (b, f, j) HAADF-STEM images. (c, g, k) Pseudo-color processing images. (d, h, l) Cd or S atom column intensities of the selected regions near sample surface.

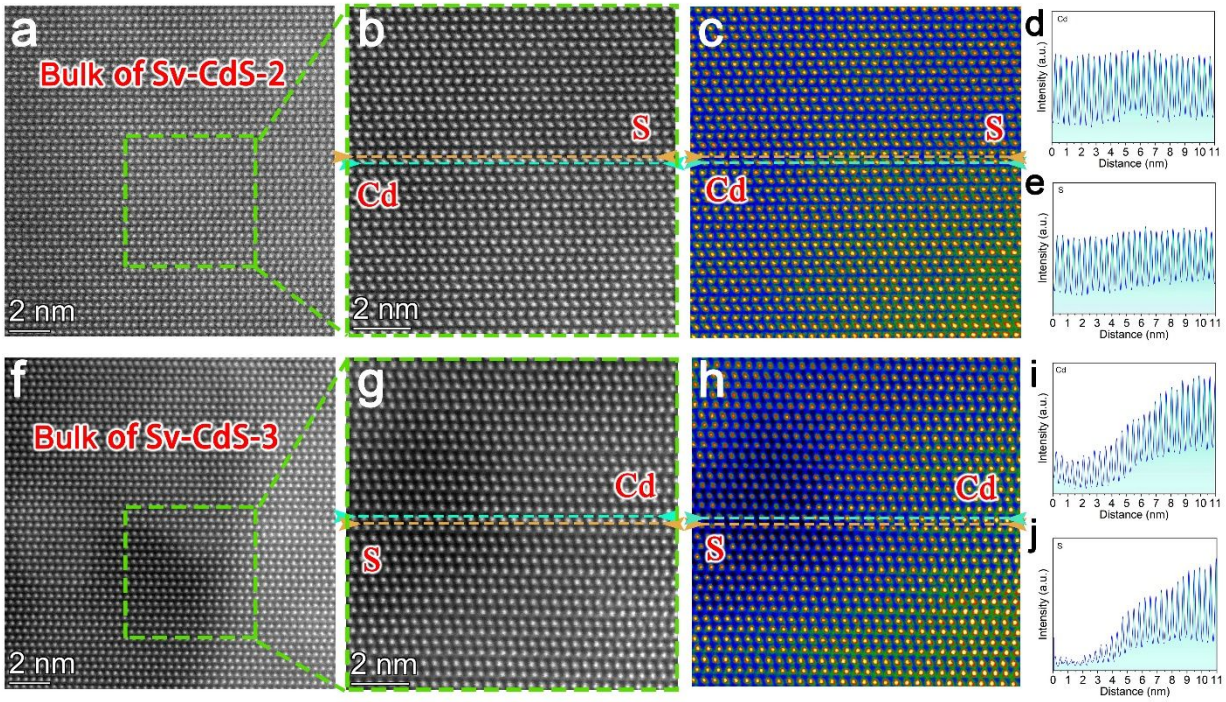

Figure S3. Structure analysis for bulk phase of Sv-CdS-2 (a-e) and Sv-CdS-3 (f-j).

Along with increasing single atomic S vacancy concentration, binding energy of S element in Sv-CdS NRs presents a gradual positive shift, indicating an electron donation state and thus a reduced electron density for S atom surroundings; while Cd element shows a negatively shifted signal with a widened half width, meaning an electronic abundance environment near Cd atoms (Figure S4a). In detail, XPS spectra of Cd 3d and S 2p were fitted (Figure S4b,c). It is seen that there is no much difference in the fitted S 2p spectra among these four samples. For Cd 3d, obviously, an additional peak in lower binding energy assigned to Cd of low valence appears gradually for Sv-CdS-1 and Sv-CdS-2 due to the generation of S vacancy, and then this peak nearly disappears in Sv-CdS-3 resulting from the formation of multi-atomic Cd-S vacancies. These results are well consistent with the HAADF-STEM observation (Figure S2i-l and Figure S3f-j).

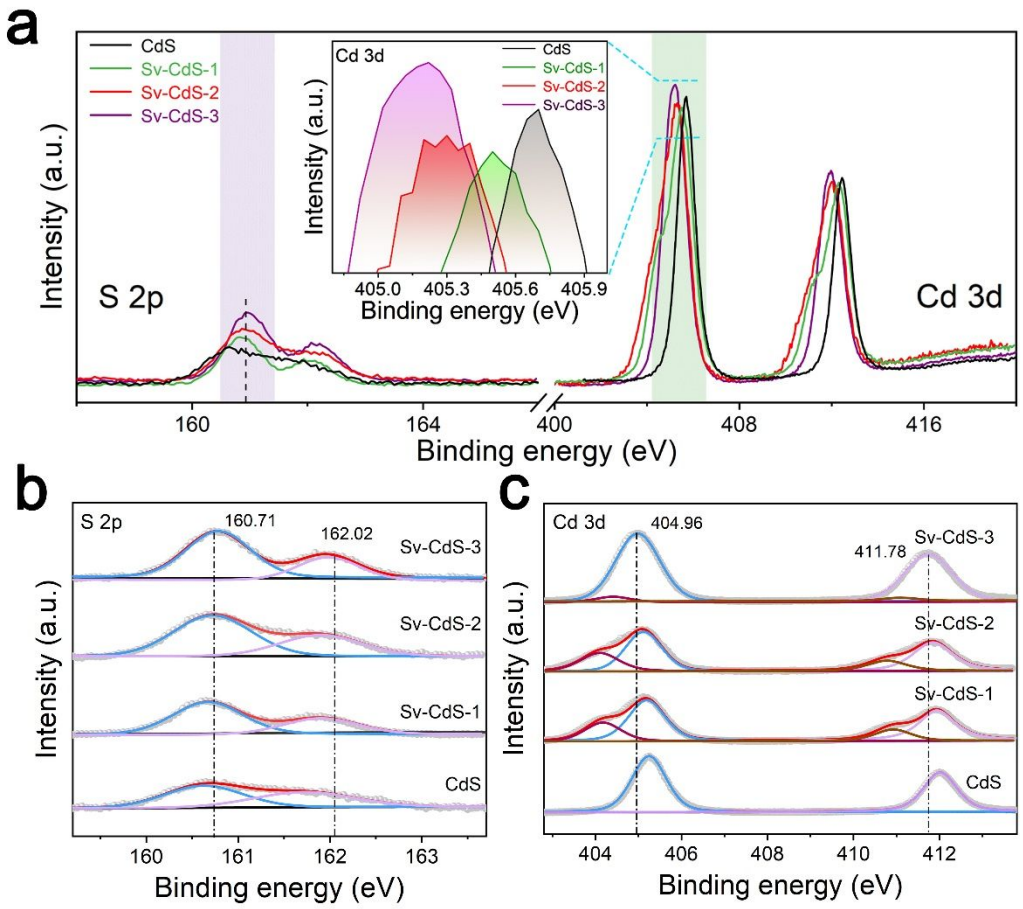

Figure S4. XPS Full spectra (a) and the fitted S 2p (b) and Cd 3d (c) spectra.

With extending the Sv-CdS unit cell to (2x2x2) and (2x2x3), Bader charge distribution on both S and Cd atoms fluctuates greatly, as is the same with CdS unit cell of (2×2×1). Cd atom neighbouring directly to S vacancy has only +0.50 e or +0.49 e charges for (2×2×2) or (2×2×3) unit cell, respectively, and even Cd atoms those are far from S vacancy have only +0.67~ +0.69 e charges (Figure S5). It is seen that S atoms present electron donation trend in these models, meaning that S vacancy induces the redistribution of unpaired spin electron and the formation of spin polarization electric field (PEF).

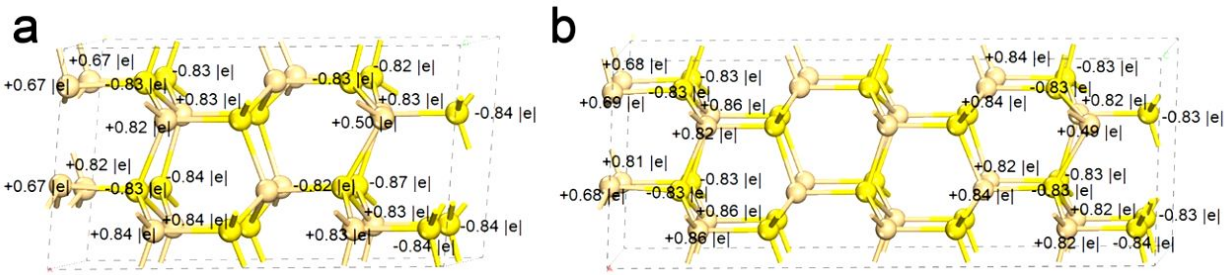

Figure S5. Bader charge distribution of S-vacancy CdS models. (a) (2×2×2) units. (b) (2×2×3) units.

Electrochemical impedance spectroscopy profiles which was used for calculation of spin PEF intensity were shown in Figure S6a. The formation of spin PEF intensity is favorable to H_2O adsorption to the region near S vacancy in Sv-CdS with a decreased adsorption energy (E_{ads}) of -0.68 eV (Figure S6b) compared with that of -0.42 eV for CdS (Figure S6c), coupling with a decreased PL intensity for Sv-CdS (Figure S6d).

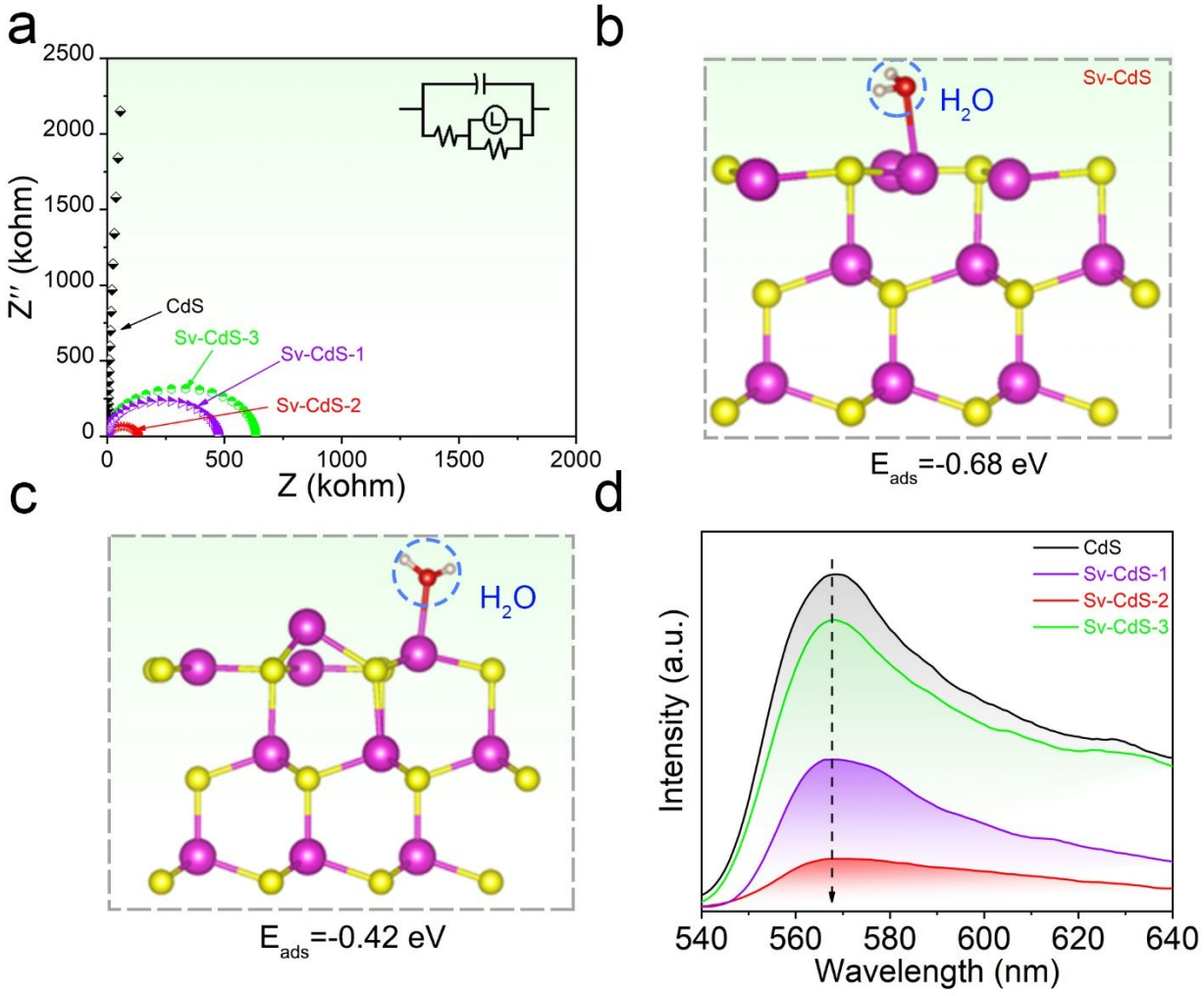

Figure S6. Spin PEF detection, H_2O adsorption and charge separation ability. (a) EIS profiles. (b) Model of H_2O adsorption on hexagonal Sv-CdS (002) plane and (c) on hexagonal CdS (002). (d) PL spectra.

The optical absorption characteristics of CdS NRs are also improved with the introduction of S vacancies due to the more involvement of S 2p orbit in the band structure of Sv-CdS as presented by TDOS and PDOS results (Figure S7).

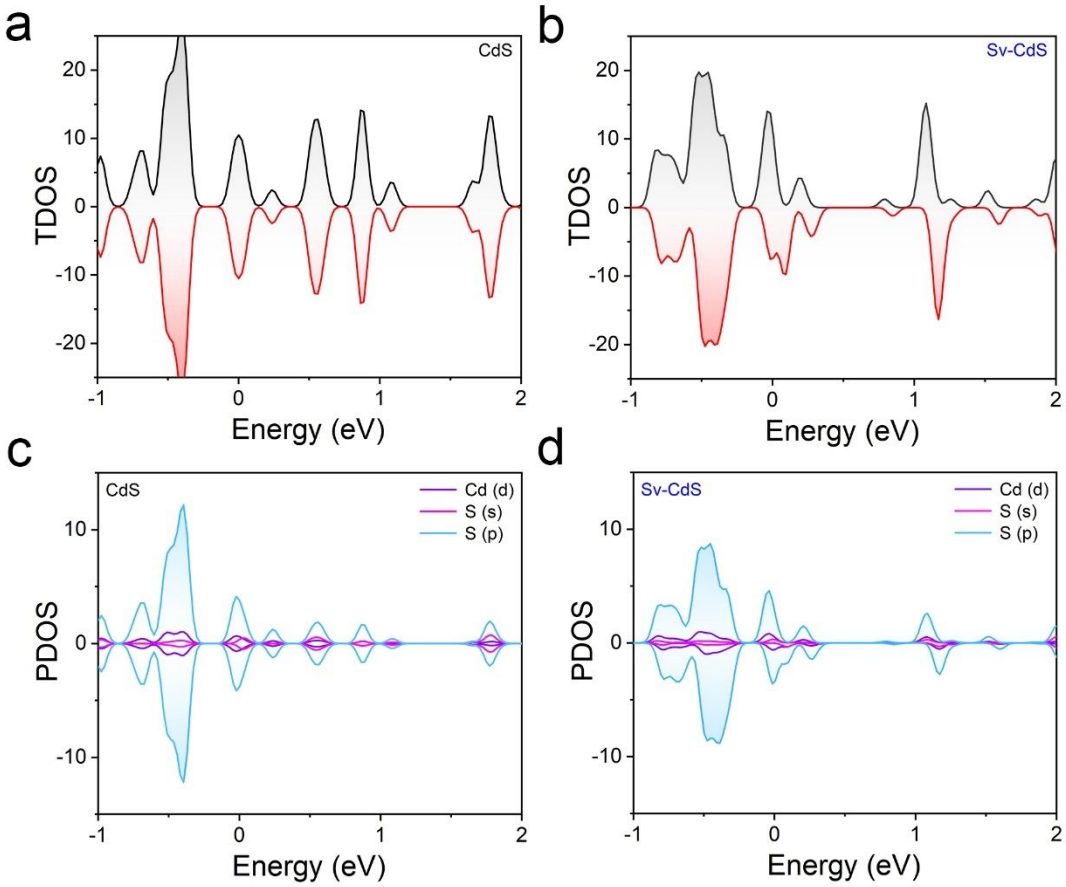

Figure S7. Band structure of CdS and Sv-CdS from theoretical calculation. (a, b) Total density of states. (c, d) Partial density of states.

The improved charge separation and transfer ability over Sv-CdS samples promote H_2O splitting with a lowered onset potential of -0.083 V presented in linear sweep voltammogram curves (Figure S8a) and Volmer reaction process is rate-limiting step in H_2O splitting over Sv-CdS-2 sample shown in the derived Tafel slopes (Figure S8b), indicating that H_2O adsorption and electron transfer play a key role in the H_2O splitting into H_2.

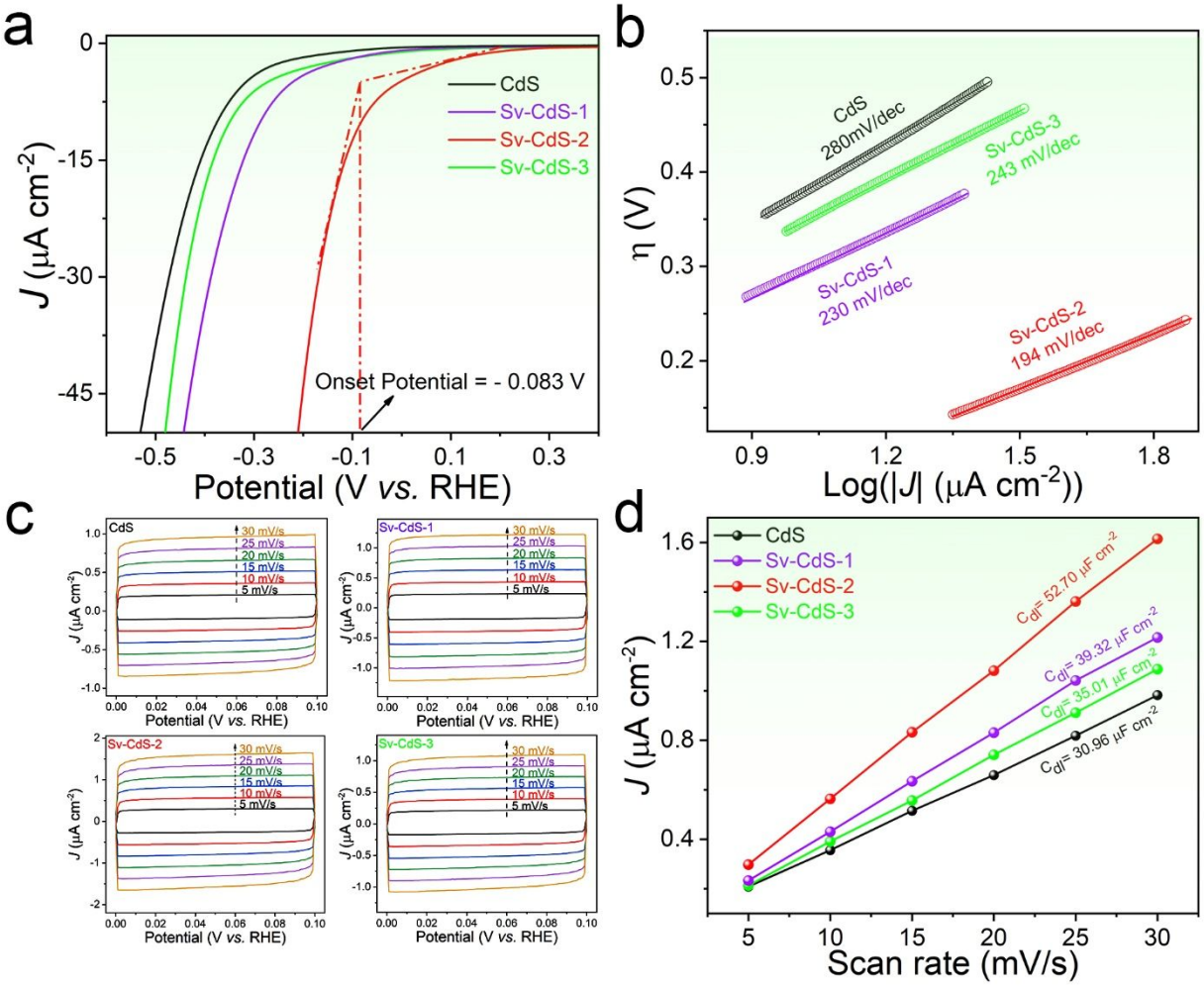

Figure S8. Electronic property. (a) Linear sweep voltammogram curves for H_2O splitting. (b) The derived Tafel slopes. (c) CV curves with different scanning rates. (d) The derived double layer.

Iodometry was operated by adding excess I_2 solution into the photocatalytic system after each recycle test to consume the residual sacrificial agents, and then the excessive I_2 was titrated by $Na_2S_2O_3$ solution. The corresponding chemical reactions were listed as follow:

$$Na_2S + I_2 = 2NaI + S \qquad \text{Equation S1}$$

$$Na_2SO_3 + I_2 + H_2O = Na_2SO_4 + 2HI \qquad \text{Equation S2}$$

$$Na_2S_2O_3 + I_2 = Na_2S_4O_6 + 2NaI \qquad \text{Equation S3}$$

The consumed rate of sacrificial agents *vs.* reaction time was plotted as Equation Figure S9c. It is seen that ~50% of sacrificial agents have been consumed after two rounds of recycle tests, which thus results in the decreased efficiency in the third test. When sacrificial agents were added into the photocatalytic system according to the consumption rate plots of sacrificial agents, H_2 evolution efficiency over Sv-CdS-2 recovered to top form again.

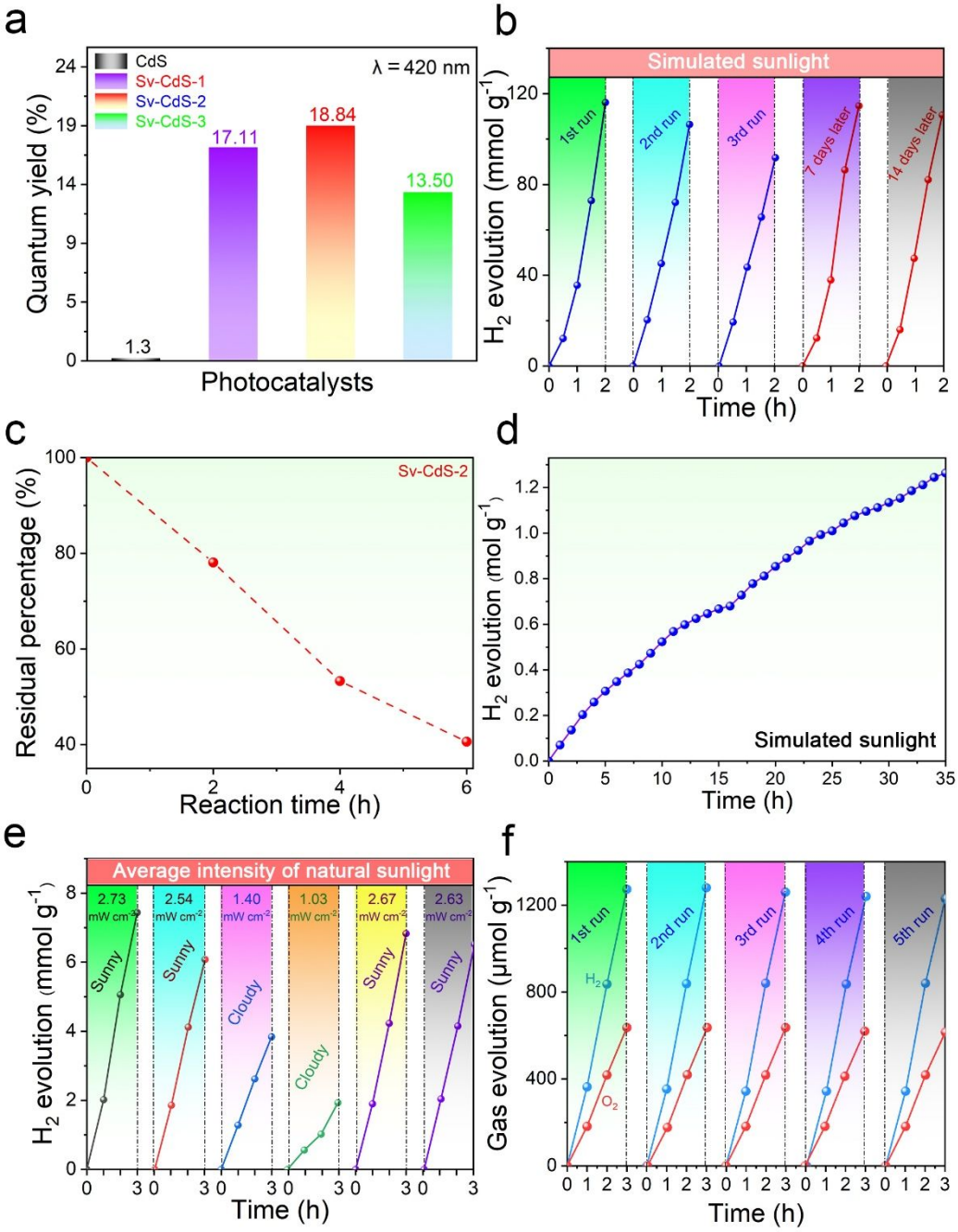

Figure S9. Long-term stability and reusability. (a) AQE of CdS and Sv-CdS samples at 420 nm. (b) Reusability stability of Sv-CdS-2 under simulated sunlight irradiation. (c) Consumption rate of sacrificial agents *vs.* reaction time. (d) Long-term photocatalytic performance of 35 h simulated sunlight irradiation. (e) Reusability stability of Sv-CdS-2 under natural sunlight

irradiation. (f) H_2O overall splitting performance of Sv-CdS-2 under simulated sunlight irradiation without sacrificial agents.

After stability tests, CdS and Sv-CdS-2 photocatalyst was collected and characterized by XRD and XPS (Figure S10). It is seen that phase structure for both CdS and Sv-CdS-2 shows no difference before and after stability tests (Figure S10a). In XPS, S2p spectrum for the recycled CdS shows an additional peak at 168.5 eV for SO_4^{2-} species compared with the fresh CdS (Figure S10b and Figure S4), indicating the structure instability of pristine CdS. In comparison, chemical states and Cd/S atom ratio of Sv-CdS-2 show no obvious change before and after recycling tests (Figure S10b, Figures S4 and Table S1). Furthermore, HAABF-STEM was used to observe S vacancy of the recycled Sv-CdS-2. Compared with Figure 1g-k results, intensities of S atom columns have no much difference after stability tests (Figure S11). This should be attributed to the highly efficient utilization of photogenerated h^+ into the oxidation of sacrificial agents or H_2O molecules, greatly restraining the oxidation of S atoms on Sv-CdS surface. Therefore, the good phase structure stability and the high utilization efficiency of photogenerated h^+ in Sv-CdS guarantee the ultrahigh long-term stability and reusability.

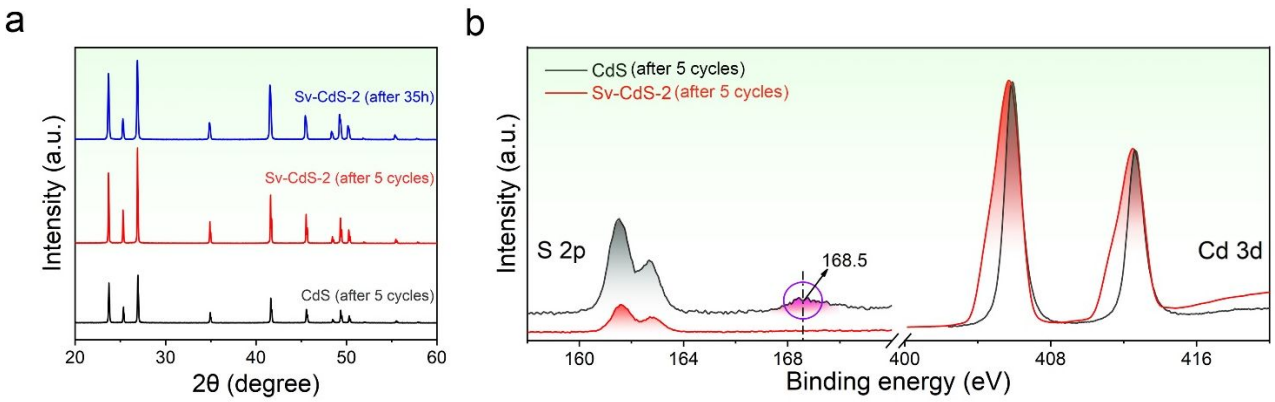

Figure S10. XRD (a) and XPS (b) profiles of the recycled CdS and Sv-CdS-2.

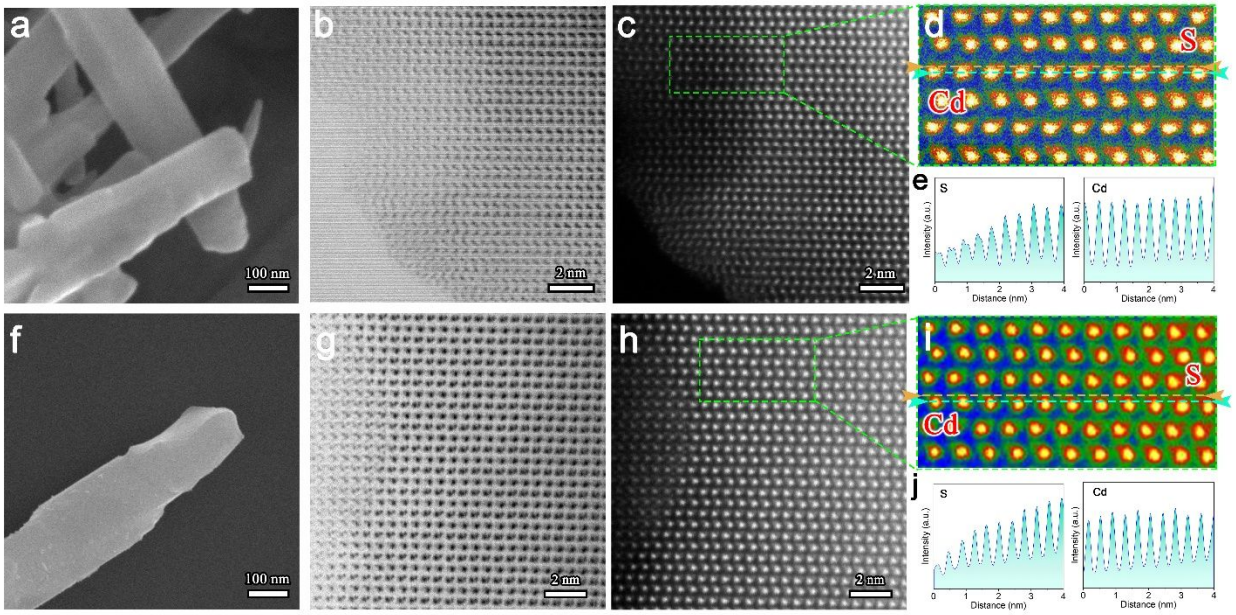

Figure S11. Structure stability of the recycled Sv-CdS-2 after photocatalytic reactions of H_2O overall splitting for 5 cycles (a-e) and 35 h (f-j). (a,f) SEM image. (b,g) HAABF-STEM image. (c,h) HAADF-STEM image and (d,i) the corresponding pseudo-color processing image as well as (e,j) Cd or S atom column intensity in the selected region.

According to Mott-Schottky plots (Figure S12) and band gap information of UV-vis DRS in Figure 3c, detailed band structure can be given as Figure 5c.

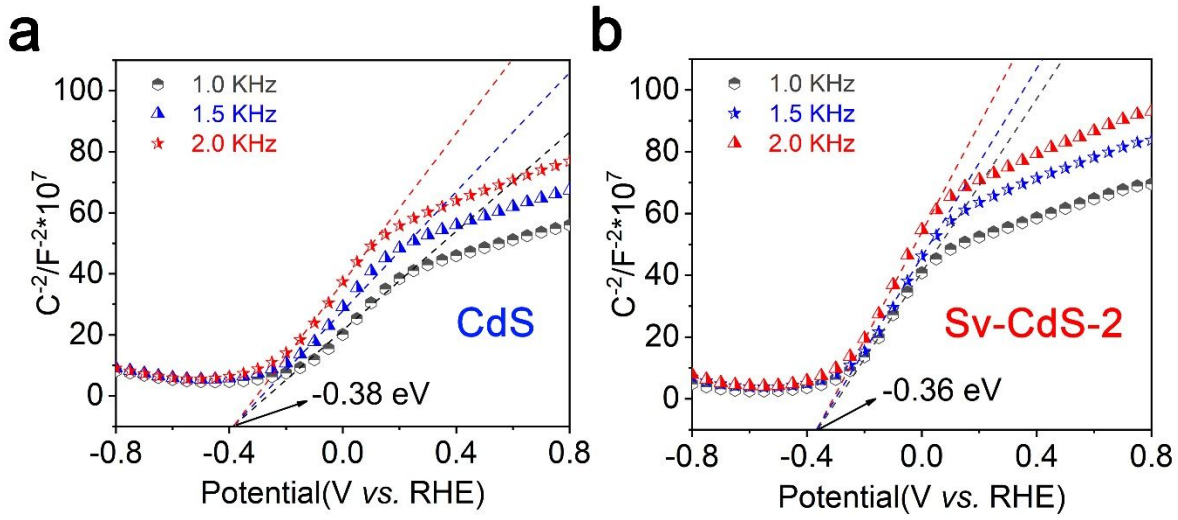

Figure S12. Mott-Schottky plots for CdS and Sv-CdS-2.

Table S1. Atomic content (at%) of S and Cd in CdS and Sv-CdS samples before and after stability tests.

Sample	XPS		ICP-OES		S vacancy content (XPS/ICP)
	S	Cd	S	Cd	
CdS	50.42	49.58	50.51	49.49	-
Sv-CdS-1	49.68	50.32	49.82	50.18	1.27/0.72
Sv-CdS-2	49.01	50.99	49.43	50.57	3.88/2.25
Sv-CdS-3	48.67	51.33	48.54	51.46	5.18/5.67
Sv-CdS-2 (After reaction)	48.99	51.01	49.41	50.59	3.96/2.33

Table S2. Fluorescence lifetime of CdS samples.

Samples	τ_1 (ns) (A_1)	τ_2 (ns) (A_2)	τ_v	k_{ent}	φ_{ent}
CdS	3.89 (83.75%)	11.05 (16.25%)	6.434	0.167	0.648
Sv-CdS-1	4.20 (75.15%)	18.15 (24.85%)	12.407	0.183	0.769
Sv-CdS-2	4.25(68.35%)	22.75 (31.65%)	17.337	0.191	0.813
Sv-CdS-3	3.85 (84.85%)	9.95 (15.15%)	5.776	0.159	0.613

The average lifetimes (τ_v), energy transfer rate (k_{ent}) and quantum yield (φ_{ent}) have been calculated according to Equation S4-6 based on the information of τ_1 (A_1) and τ_2 (A_2). [S6]

$$\tau_v = \frac{\tau_1^2 \times A_1 + \tau_2^2 \times A_2}{\tau_1 \times A_1 + \tau_2 \times A_2} \quad \text{Equation S4}$$

$$k_{ent} = \frac{1}{\tau_1} - \frac{1}{\tau_2}$$ Equation S5

$$\varphi_{ent} = \frac{k_{ent}}{\tau_1}$$ Equation S6

Equation used for Applied Bias Photon-to-Current Efficiency (ABPCE) calculation.

ABPCE was calculated by Equation S7.[S7]

$$\eta = \frac{I(1.23 - V)}{J_{light}} \qquad \text{Equation S7}$$

η is ABPCE, V is the applied bias *vs.* RHE, I is the photocurrent density at the measured bias, and J_{light} is the irradiance intensity of 40 mW/cm^2.

Table S3. The detailed experimental conditions of the references cited in Figure 4c of the main text.

Photocatalysts	wavelength	concentration of sacrificial agents	intensity of light	area of light irradiation	Ref.
TiO_2/MoS/CdS	$\lambda \geq 400$ nm	10 vol% lactic acid aqueous solution	300 W Xe lamp	-	33
PVDF-HFP/CdS-Pt	full spectrum	15wt.% TEA aqueous solution	280 W Xe lamp	-	34
CdS/MoO_X	$\lambda \geq 400$ nm	10 vol% lactic acid aqueous solution	300 W Xe lamp	-	35
Sn^{2+}/CdS QDs	$\lambda \geq 420$ nm	glycerol	350 W Xe lamp	-	36
CdS/GNR	$\lambda \geq 400$ nm	10 vol% lactic acid aqueous solution	300 W Xe lamp	-	37
CdS/CoS_2	-	20 vol% ascorbic acid aqueous solution	A full spectrum solar simulator (about 1 Sun power)	17.8 cm^2	38
CdS frame-in-cage particles	$\lambda \geq 400$ nm	0.35 M of Na_2S 0.25 M of Na_2SO_3	300 W Xe lamp	-	39
CdS-$Cu_{2-X}S$/MoS_2	$\lambda \geq 400$ nm	0.75 M of Na_2S 1.05 M of Na_2SO_3	300 W Xe lamp	-	40
NiS/ZnCdS MOF	$\lambda \geq 420$ nm	0.35 M of Na_2S 0.25 M of Na_2SO_3	300 W Xe lamp	-	41
Ni/ZCS QDS	$\lambda \geq 420$ nm	20 vol% TEOA aqueous solution	300 W Xe lamp	-	22
$Cd_{0.5}Zn_{0.5}S$@halloysite	$\lambda \geq 420$ nm	0.1 M of Na_2S 0.1 M of Na_2SO_3	300 W Xe lamp		42
BP-Au-CdS	-	0.35 M of Na_2S 0.25 M of Na_2SO_3	300 W Xe lamp	-	43
CdS(111)	$\lambda \geq 420$ nm	0.35 M of Na_2S 0.25 M of Na_2SO_3	350 W Xe lamp	-	15
CdS/CoS_X	$\lambda \geq 420$ nm	0.35 M of Na_2S 0.25 M of Na_2SO_3	300 W Xe lamp	-	44
Pd@CdS/PdS	$\lambda \geq 400$ nm	0.1 M of Na_2S 0.1 M of Na_2SO_3	300 W Xe lamp	-	45
InP/ZnS QDS	$\lambda = 525$ nm	0.035 mM $NiCl_2 \cdot 6H_2O$ 0.2 M H_2A/NaHA	4*1 W LED	-	46
Cu-Zn-Ga-S	$\lambda \geq 420$ nm	0.35 M of Na_2S 0.25 M of Na_2SO_3	300 W Xe lamp	-	47
ZnS/CoS_2	$\lambda \geq 400$ nm	0.2 M of Na_2S 0.2M of Na_2SO_3	100 W Xe lamp	-	48
ReS_2	$\lambda \geq 420$ nm	0.35 M of Na_2S 0.25 M of Na_2SO_3	300 W Xe lamp	-	49
Co_9S_8/$ZnIn_2S_4$	$\lambda \geq 400$ nm	10 vol% triethanolamine aqueous solution	300 W Xe lamp	-	50
MoS_2 QDS@VS-M-$ZnIn_2S_4$	$\lambda \geq 400$ nm	10 vol% lactic acid aqueous solution	300 W Xe lamp	-	51
$Eu_{52}Ni_{56-X}Cd_X$	$\lambda \geq 420$ nm	0.35 M of Na_2S 0.25 M of Na_2SO_3	300 W Xe lamp	-	52
This work	$\lambda \geq 420$ nm	0.35 M of Na_2S 0.25 M of Na_2SO_3	350 W Xe lamp	12.56 cm^2	-

REFERENCES FOR SUPPORTING INFORMATION

(1) Perdew, J. P.; Burke, K.; Ernzerhof, M. Generalized Gradient Approximation Made Simple. *Phys. Rev. Lett.* **1996**, *77* (18), 3865.

(2) Kresse, G.; Joubert, D. From Ultrasoft Pseudopotentials to the Projector Augmented-Wave Method. *Phys. Rev. B* **1999**, *59* (3), 1758.

(3) Blöchl, P. E.; Jepsen, O.; Andersen, O. K. Improved Tetrahedron Method for Brillouin-Zone Integrations *Phys. Rev. B* **1994**, *49* (23), 16223.

(4) Kresse, G.; Furthmüller, J. Efficient Iterative Schemes for *ab Initio* Total-Energy Calculations Using a Plane-Wave Basis Set. *Phys. Rev. B* **1996**, *54* (16), 11169.

(5) Kresse, G.; Furthmüller, J. Efficiency of *ab-Initio* Total Energy Calculations for Metals and Semiconductors Using a Plane-Wave Basis Set. *Comput. Mater.Sci.* **1996**, *6* (1), 15-50.

(6) D'Souza, F.; Smith, P. M.; Zandler, M. E.; McCarty, A. L.; Itou, M.; Araki, Y.; Ito, O. Energy Transfer Followed by Electron Transfer in a Supramolecular Triad Composed of Boron Dipyrrin, Zinc Porphyrin, and Fullerene: A Model for the Photosynthetic Antenna-Reaction Center Complex *J. Am. Chem. Soc.* **2004**, *126* (25), 7898-7907.

(7) Yang, C.; Wang, Z.; Lin, T.; Yin, H.; Lü, X.; Wan, D.; Xu, T.; Zheng, C.; Lin, J.; Huang, F. Core-Shell Nanostructured “Black” Rutile Titania as Excellent Catalyst for Hydrogen Production Enhanced by Sulfur Doping. *J. Am. Chem. Soc.* **2013**, *135* (47), 17831-17838.